N-terminal region of PetD is essential for cytochrome *b₆f* function and controls STT7 kinase activity via STT7-dependent feedback loop phosphorylation

Afifa Zaeem[1], Yuval Milrad[1], Simon Bütfering[1], Carolyne Stoffel[2], Adrien Burlacot[2,3], Martin Scholz[1], Felix Buchert[1*], Michael Hippler[1,4*]

[1]Institute of Plant Biology and Biotechnology, University of Münster, 48143 Münster, Germany
[2]Biosphere Sciences and Engineering Division, Carnegie Science, Stanford, CA 94305
[3]Department of Biology, Stanford University, Stanford, CA 94305
[4]Institute of Plant Science and Resources, Okayama University, Kurashiki, Japan

[*]Correspondence to: felix.buchert@uni-muenster.de; mhippler@uni-muenster.de

Abstract

The cytochrome *b₆f* complex (*b₆f*) links photosystem I (PSI) and photosystem II (PSII) in the photosynthetic electron transport chain and is distributed across appressed and non-appressed thylakoid membranes. The *b₆f* also activates the state-transition 7 kinase (STT7), which phosphorylates light-harvesting complex proteins, triggering their migration to enable energy redistribution between PSII and PSI. STT7-dependent phosphorylation has also been observed at T4 in the N-terminal domain of the *b₆f* subunit-IV (PetD), though its functional significance has remained unclear. To investigate its role, we generated several chloroplast mutants. The phosphomimic mutation PetD T4E – but not T4A – inhibited STT7 kinase activity, as indicated by the absence of STT7-dependent phosphorylation and a State 1-locked phenotype. This reveals a novel feedback mechanism regulating STT7-dependent phosphorylation. Deletion of the first five N-terminal amino acids similarly inhibited STT7 activity and additionally disrupted electron transfer, underscoring a crucial role of the PetD N-terminus in *b₆f* function.

32 **Main**

33 Photosynthesis captures light through photosystem (PS) I and PSII along with light-harvesting
34 complexes (LHCI and LHCII). Light energy drives water splitting at PSII and ultimately
35 reduces ferredoxin (FDX) through PSI. In linear electron flow (LEF), reduced FDX transfers
36 electrons to FDX-NADP(H) oxidoreductase (FNR), producing NADPH for CO_2 fixation and
37 biomass production. In addition, electron transport deposits H^+ in the lumen and separates
38 charges across the thylakoid membrane, thereby generating both a proton gradient (ΔpH) and
39 membrane potential (ΔΨ), which collectively drive ATP synthesis. Electron flow between the
40 photosystems is mediated by the cytochrome *b₆f* complex (*b₆f*; reviewed in [1]), which shuttles
41 electrons from plastoquinol (PQH_2) in the plastoquinone (PQ) pool to plastocyanin. Besides
42 small peripheral subunits, the *b₆f* core comprises cytochrome-*f* (PetA), cytochrome-*b₆* (PetB),
43 Rieske iron-sulfur protein (ISP, PETC), and subunit-IV (PetD). Electron flow through the
44 high-potential chain, involving PETC and PetA, is functionally linked to redox reactions in
45 the low-potential chain of PetB, including the heme c_i cofactor at the Qi-site. The Qi-site
46 serves as the stromal binding pocket for PQ, whereas PQH_2 binds at the lumenal Qo-site. By
47 translocating protons into the lumen through reversible PQ protonation at the Qi and Qo sites,
48 the ΔpH generated by *b₆f* activity substantially contributes to ATP production required for
49 CO_2 fixation. Moreover, the c_i heme within the Qi-site is relevant for cyclic electron flow
50 (CEF) and the *b₆f* complex may function as a FDX-PQ reductase (FQR) in CEF [2,3].

51 The lumen acidification stemming from photosynthetic electron flows is important for
52 efficient photoprotection under conditions of excess excitation energy: it establishes
53 "photosynthetic control" at the Qo-site where PQH_2 oxidation (and therefore electron flow)
54 slows down at acidic pH [4,5], and it decreases photochemistry by stimulating controlled heat
55 dissipation via non-photochemical quenching (NPQ) [6-8]. Moreover, the *b₆f* is linked to state
56 transitions – another photoprotective mechanism to cope imbalanced excitation [9]. During this
57 process, LHCII migrates between PSII and PSI upon its phosphorylation by the thylakoid-
58 bound STT7 kinase [10,11]. STT7 is activated by a reduced PQ pool while specific phosphatases
59 act as STT7 antagonists [12]. The activity of the STT7 kinase is regulated by its transmembrane
60 domain, with a disulfide bond between two lumenal cysteine residues being essential for its
61 function [13]. Active discussions and research on the kinase redox regulation are ongoing [14-16].
62 Recently it was shown that state transitions involve PetD residues N122, Y124, and R125 in
63 the stromal "fg Loop", linking helices F and G of this *b₆f* subunit [17]. Moreover, the C-
64 terminus of the *b₆f* subunit PetB ($PetB^{C\text{-}term}$) interacts with the fg Loop in PetD, thereby
65 facilitating STT7 activation [18]. Mechanistically, the fg Loop and $PetB^{C\text{-}term}$ allow for binding
66 of STT7 to *b₆f* which enhances kinase autophosphorylation. In this report we focus on another
67 stromal element of *b₆f* in the model green microalgae *Chlamydomonas reinhardtii* (see
68 Extended data Fig. 1): The N-terminus in PetD, where T4 undergoes phosphorylation in an
69 STT7-dependent manner [19] (see also Extended data Fig. 2).

PetD T4 phosphorylation has been described by several groups [19,20] and to investigate the functional significance of STT7-dependent phosphorylation at PetD T4, we created PetD site-directed mutants T4A and T4E via chloroplast transformation to mimic constitutive absence and presence of phosphorylation, respectively. Moreover, the function of the five N-terminal residues was addressed in a truncation mutant (ΔN) whereas the wild-type PetD (WT) was used as control. The *petD* recipient strain carried a six-histidine tag at the C-terminus of PetA [21] for optional b_6f purification. Spot test on agar plates, requiring photoautotrophic growth, revealed that mutant strains T4A and T4E performed similar to WT under normal light (40 µmol photons m^{-2} s^{-1}, Extended data Fig. 3a). In moderate high light (200 µmol photons m^{-2} s^{-1}; Extended data Fig. 3a), T4E revealed a severe growth phenotype in comparison to T4A and WT. In contrast, the ΔN strain showed a growth deficit at both light intensities compared to the other strains. Proteomic analyses showed no significant differences in the levels of PetD and other core b_6f subunits between WT, T4A, and T4E. In contrast, most of these subunits were slightly depleted in ΔN, and the CEF effector protein PETO [22] was significantly downregulated (Extended data Fig. 3b). LHCSR1 – required for pH-dependent NPQ [23] – was markedly upregulated in T4E relative to T4A (Extended data Fig. 4). Moreover, STT7 peptide abundance was slightly lower in T4E compared to the similar levels observed in the other PetD variants (Extended data Fig. 5a). Given the observed growth and protein abundance phenotypes, key photoprotection pathways associated with b_6f function might be altered in the mutants. To this end, we first present data investigating state transitions as they require the physical presence of b_6f [24], and then performed electron transfer measurements to directly assess b_6f activity in the mutants.

To explore if state transitions are affected in the mutants, the antenna redistribution between PSI and PSII was measured using 77 K fluorescence emission spectroscopy [25] after cells were shifted to either State 1 or State 2 inducing conditions (Fig. 1a–1d). Thereby, an increase in PSI-associated antennae size under State 2 versus State 1 conditions was observed for WT and T4A (Figs. 1a, 1b). In contrast, T4E and ΔN strains displayed no differences in their 77 K fluorescence emission spectra, indicating they were unable to perform state transitions (Figs. 1c, 1d). Using electrochromic shift (ECS) signals [26], we also followed the transition from State 2 to State 1 upon continuous illumination when PSII was inhibited (Fig. 1e). Thereby, we monitored the progressive reduction of PSI antenna size and, while this was seen in WT and T4A, a significant impairment was detected in T4E and ΔN (Fig. 1f). The ECS-based state transitions amplitudes in WT were comparable to those reported in literature [27], whereas T4A showed a reduced ability to revert to State 1 (Fig. 1g). The relative changes in both T4E and ΔN were the smallest.

The data in Fig. 1 suggest impaired STT7-dependent phosphorylation in both T4E and ΔN strains. To define specific STT7-dependent phosphorylation targets, we conducted phosphoproteomic analyses including a novel CRISPR/Cas9-generated *STT7* knockout

mutant (Extended data Fig. 6). This *STT7* mutant served both as a benchmark reference for the PetD strains and as a tool to distinguish between effects stemming from different genetic *STT7* backgrounds (see also Extended data Table 1). To dissect STT7 function, cf. Fig. 2 and Extended data Fig. 2, as well as the following selection of results loosely categorized into five groups: (*i*) kinase autophosphorylation, (*ii*) LHCII and state transition complex formation, (*iii*) photoprotective CEF and NPQ, (*iv*) b_6f and photosystem core subunits, and (*v*) miscellaneous phosphorylation targets.

An unexpected [19] observation was that, unlike *STT7*, the ΔN and T4E strains showed no detectable changes in LHCSR3 (T32) or LHCB4 double (T7+T11) phosphorylation. As these phosphorylation events are interrelated [28], this suggests either residual STT7 activity in ΔN and T4E, or a compensatory mechanism involving the physical presence of STT7 and possibly other chloroplast kinases such as STN8. Supporting the latter hypothesis, STN8 phosphorylation at T126 – absent in *STT7* – was retained in both ΔN and T4E, hinting at an intricate and potentially compensatory kinase network.

(*i*) STT7 phosphorylation at S569/T571 was severely reduced in ΔN and T4E (Extended data Figs. 5b–5c), consistent with their failure to undergo state transitions. Nonetheless, STT7 autophosphorylation at T511, T513, T516, S533, and T547 remained largely unchanged across all strains (Extended data Figs. 5d–5h), suggesting that STT7 is partially functional in ΔN and T4E.

(*ii*) In *STT7*, phosphorylation was broadly lost across key threonine clusters [28], notably the double phosphorylation in LHCB4 (T33+T35, T33+T37, T35+T37) and phosphorylation of T23 and T36 in LHCB5 (Extended data Table 1). LHCB5 retained only minimal phosphorylation at T20, and LHCB4 double-phosphorylation at T7+T11 was reduced by 6.8 $\log_2$-fold. Several background-independent [19,29] phosphorylation sites absent in *STT7* were also either absent (T27 of LHCBM1) or strongly diminished (double phosphorylation of S28+T33 in LHCBM5) in ΔN and T4E. The altered N-terminal phosphorylation in LHCBM1 and LHCBM5 likely explains the loss of state transitions in both strains, as these modifications are essential for assembly of the PSI–LHCI–LHCII state transition complex [30].

(*iii*) As mentioned above, *STT7* lacked phosphorylation in the LHCSR3 N-terminal cluster (S26/S28/T32/T33/T39) [28], where up to three simultaneously phosphorylated residues were observed in WT. Meanwhile, LHCSR3 phosphorylation showed no significant difference between WT and the PetD variants. In contrast, ANR1 phosphorylation at T171 was confirmed to be a background-independent [19,29] target of STT7. It was also undetectable in ΔN and T4E. Notably, PETO levels were reduced nearly five-fold in ΔN (Extended data Fig. 3b). Given that PETO can chemically crosslink to K15 in the N-terminal region of PetD [31], its loss in ΔN and fg-loop mutants [18] supports a functional PetD–PETO interaction. Disruption of this interaction likely triggers PETO degradation.

(*iv*) Consistent with prior data from an independent *STT7* mutant [19], PetD T4 phosphorylation was absent in *STT7*, while PSBD (T2) phosphorylation was markedly elevated (5.5 $\log_2$-fold).

147 T4E exhibited a similar increase (3.4 $\log_2$-fold), whereas ΔN and T4A showed no significant
148 changes at PSBD (T2). Both ΔN and T4E displayed reduced phosphorylation at PSB34 (T39),
149 PSAG (T71), and PSBR (T37, S43, T37+S43), while ΔN specifically showed increased
150 phosphorylation at PSAG T72. T4A, in contrast, exhibited a distinct profile: most
151 phosphorylation sites were unchanged, but PSBR phosphorylation (T37, S43, T37+S43) was
152 significantly elevated compared to the other strains.
153 (*v*) PTAC16 – a component of the plastid transcriptionally active chromosome complex and a
154 known STN7 substrate in *Arabidopsis* [32,33] – displayed the highest number of differentially
155 phosphorylated sites. In *STT7*, PTAC16 phosphorylation was largely abolished. Similar
156 patterns were observed in ΔN and T4E, though both retained some WT-specific
157 phosphorylation. In contrast, the T4A mutant showed no significant changes in PTAC16
158 phosphorylation.
159 To assess functional consequences of the alterations in the engineered strains, we measured
160 photosynthetic electron transfer rates (ETR) using ECS signals. The measured ETR in T4A
161 and T4E were indistinguishable from WT, suggesting that phosphorylation at T4 does not
162 have a direct impact (Figs. 3a, 3b). In contrast, ΔN cells showed a marked slowdown in ETR
163 30–50 ms after light onset under oxic conditions (Fig. 3a). Under anoxic conditions that
164 favour CEF, ETR initially increased but reached a lower steady state, with the initial boost
165 markedly reduced in ΔN compared to the other strains (Fig. 3b), indicating that the PetD N-
166 terminus supports ETR via the b_6f. Redox kinetics of P700 were also assessed (Figs. 3c, 3d).
167 In ΔN, P700 oxidized rapidly upon illumination and re-reduced slowly in the dark, consistent
168 with donor-side limitation under both oxic and anoxic conditions. Notably, steady-state ETR
169 (Figs. 3a, 3b) were established despite substantial P700 acceptor-side limitation in all strains
170 except in ΔN (Figs. 3c, 3d). This persistent donor-side limitation in ΔN was unaffected by the
171 addition of the H^+/K^+ exchanger nigericin (Extended data Figs. 7a, 7b), excluding pH-
172 dependent photosynthetic control. Treatment with DCMU and nigericin led to rapid P700
173 oxidation in all strains, slightly faster in ΔN (Extended data Figs. 7c, 7d), supporting impaired
174 b_6f function in both LEF and CEF.
175 To confirm whether the observed differences ETR and P700 redox kinetics differences
176 stemmed from b_6f dysfunction, we evaluated b_6f electrogenicity and redox kinetics (Extended
177 data Fig. 8a, Fig. 4). ECS rise linked to Q-cycle activity was impaired exclusively in ΔN,
178 despite the presence of heme c_i – the terminal electron acceptor in the low-potential chain [34] –
179 as well as WT-like stability of the truncated b_6f complex (Extended data Figs. 8b–c). Under
180 oxic conditions (Fig. 4a), WT *b*-hemes showed a transient reduction (~10 ms) before net
181 oxidation (~16 ms half-life), while cytochrome-*f* reduction (~6 ms half-life) began ~1 ms
182 post-flash. In ΔN, the apparent *b*-heme reduction was enhanced because their oxidation
183 slowed ~20-fold (Fig. 4b). This coincided with a ~10-fold slowdown in cytochrome-*f*
184 reduction, indicating Qi-site impairment affecting the Qo-site as has been shown in b_6f [3,35] and
185 the related cytochrome-bc_1 complex [36,37]. Under anoxic conditions (Fig. 4c), WT displayed

186 flat *b*-heme signals in the first 10 ms, followed by accelerated oxidation, consistent with prior
187 findings [3,35]. In ΔN, a redox-inactive low-potential chain caused a ~25-fold slowdown in the
188 high-potential chain, as reflected in cytochrome-*f* reduction (cf. Figs. 4c, 4d).
189 The PetD N-terminus we investigated is exposed to the aqueous phase, contains two lysine
190 residues, and is located near PetD D35. The latter is suggested to donate a proton to a water
191 molecule in the Qi-site, which becomes displaced upon PQ binding [38]. We propose that the
192 ΔN truncation subtly affects the environment of the water channel or the functional properties
193 of PetD D35. These changes may impair electron exchange in the low-potential chain, which
194 could explain the pronounced slowdown in b_6f turnover at both Qi- and Qo-sites (Fig. 4,
195 Extended data Fig. 8a). This slowdown is consistent with the diminished ETR, enhanced
196 P700 donor-side limitation (Fig. 3), and growth retardation observed in ΔN (Extended data
197 Fig. 3a). Furthermore, diminished PQH_2 oxidation at the Qo-site impedes STT7 activation [39],
198 which may account for the partial inactivation of the kinase in the ΔN mutant (Fig. 2a).

199 In contrast to ΔN, the phosphomimic T4E mutation does not affect b_6f function. However,
200 both mutations interfere with STT7 function, albeit through distinct and likely partial
201 mechanisms: Qo-site defect in ΔN and negative charge introduction in the PetD stromal part
202 at T4E.

203 To better understand the basis of STT7 inactivation, we analyzed its autophosphorylation
204 pattern. Riche et al. [18] demonstrated via PhosTag PAGE that multiple STT7
205 autophosphorylation events are required for kinase activation, and that this process depends
206 on binding of STT7 to b_6f. Phosphorylation at residues S569 and T571 was strongly reduced
207 in both ΔN and T4E strains, whereas other autophosphorylation sites, including
208 T511/T513/T516, S533, and T547, were unaffected (Extended data Figs. 5d–5h). This data
209 suggests that STT7 remains associated with the b_6f complex in both mutant backgrounds but
210 fails to undergo full activation. The partial autophosphorylation pattern lacking residues S569
211 and T571 likely contributes to the reduced kinase activity observed. However, we cannot
212 exclude that STT7 binding to b_6f is impaired in the two mutants.

213 Our findings point to a novel feedback mechanism in which STT7 activity is modulated by
214 PetD T4 phosphorylation (Extended data Fig. 1). This feedback mechanism complements
215 previously described STT7 autophosphorylation pathways involving other stroma-exposed
216 structures of the b_6f complex[17,18]. In some cases, such as PSBR, T4A mutants displayed
217 elevated phosphorylation levels, consistent with disrupted feedback regulation. Two models
218 may explain this phenomenon: (*i*) STT7 bound to b_6f may detect PetD T4 phosphorylation
219 and respond by reducing its own autophosphorylation, leading to decreased activity. (*ii*)
220 Alternatively, STT7-dependent phosphorylation of PetD T4 could hinder subsequent STT7
221 binding to the b_6f complex, thus indirectly limiting further kinase activation.

222 In conclusion, we show that the N-terminal region of PetD is critical for b_6f function but not
223 for complex stability, and that phosphorylation at PetD T4 regulates STT7 kinase activity via
224 a novel autoregulatory feedback loop. This regulatory mode appears absent in organisms such

225 as cyanobacteria[40] and diatoms[41], which lack PetD T4 and where state transitions are
226 differently realized (Extended data Fig. 9). In Viridiplantae, feedback suppression of STT7
227 via PetD T4 may help coordinate state transitions with alternative regulatory mechanisms,
228 including those targeting PSII core subunits such as PSBD T2 [42,43].
229

230 **Methods**
231

232 **WT Plasmid construction**

233 The *petD/trnR1* region (481 bp upstream and 1032 bp downstream of *petD*) was amplified
234 from WT chloroplast DNA using restriction site-containing primer 1 (*SalI*) and 2 (*EcoRI*; for
235 oligo sequences, see Extended data Table 1). The *SalI*/*EcoRI* digested PCR product was
236 ligated into a double-digested pUC18 cloning vector and propagated as pUC18-3'-*petD*-5' in
237 NEB 5-alpha *E. coli* cells using ampicillin selection. In the next step, the aminoglycoside
238 adenyl transferase (aadA) spectinomycin resistance cassette [44] was amplified from a pUC18-
239 aadA vector using primers 3 and 4, each containing a *SpeI* restriction site. The cloned
240 *petD/trnR1* region contains a single *SpeI* site into which the aadA cassette was cloned. To do
241 so, intermediate vectors were created. First (pUC18-int1), the *SalI/SpeI* fragment from
242 pUC18-3'-*petD*-5' (1.46 kb) was ligated with the *SpeI* digested aadA PCR fragment, followed
243 by PCR (primers 1 and 5) and blunt ligation of the ~3 kb product into *SmaI* digested empty
244 pUC18 vector. Second (pUC18-int2), the *EcoRI/SpeI* fragment from pUC18-3'-*petD*-5' (0.51
245 kb) was ligated with the *SpeI* digested aadA PCR fragment, followed by PCR (primers 2 and
246 6), *XmaI*/*EcoRI* digest of the ~2 kb product, and ligation into an empty pUC18 vector. The 2.4
247 kb fragment of *BamHI*/*BlpI* digested pUC18-int1 was ligated with the 3.7 kb fragment of
248 *BamHI*/*BlpI* digested pUC18-int2 to yield pUC18-3'-*petD*-aadA-5'
249

250 **Point Mutation and Truncation Plasmid Construction**

251 To generate T4E and T4A mutation as well as the *petD* truncation ΔN (lacking underlined N-
252 terminal amino acids M<u>SVTKK</u>PD…), primers 8-11 and 13 were phosphorylated. Using
253 pUC18-3'-*petD*-aadA-5' as a template, five independent PCRs were done with the following
254 primers: 1 and 8 (I), 1 and 9 (II), 1 and 10 (III), 11 and 12 (IV) and 12 and 13 (V). Ligated
255 PCR fragments I and IV served as templates for the T4E PCR (primers 1 and 12) which was
256 further digested (*PacI*/*SalI*) for ~1.36 kb insert swapping and mutant introduction into
257 pUC18-3'-*petD*-aadA-5' (ligation with ~4.78 kb backbone). In a similar fashion, for T4A
258 PCR (primers 1 and 12) PCR fragments II and IV served as templates. For ΔN PCR (primers
259 1 and 12), fragments III and V served as templates.
260

261 **Biolistic Transformation of WT Strain**

262 Mutant strains were generated through chloroplast transformation using plasmids containing
263 the modified *petD* gene version along with an *aadA* cassette to confer spectinomycin

264 resistance (150 µg/ml). The recipient wild-type (WT) strain carries a six-histidine tag at the
265 C-terminus of PetA [21]. Spectinomycin resistant clones were selected and replated several
266 times to obtain homoplastic strains (for sequencing primers, see Extended data Table 1).
267

268 **Growth conditions and treatments**

269 Cells were maintained at 50 µmol photons m^{-2} s^{-1} at 23°C on agar plates of Tris-acetate-
270 phosphate (TAP) medium or Tris-minimal medium (TP) in the absence of acetate [45] by
271 bubbling sterile air under a 16-h light/8-h dark regime. For state transition treatment using
272 77K fluorescence, TAP-grown synchronized cultures were freshly diluted one day before the
273 experiment and, upon harvesting (4000 *g*, 5 min, 23°C), adjusted to 5 µg chlorophyll ml^{-1}.
274 Aliquots were either kept for 45 min in aerobic conditions by shaking in 40 µmol photons m^{-2}
275 s^{-1} light upon adding 10 µM 3-(3,4-Dichlorophenyl)-1,1-dimethylurea (DCMU; State 1), or
276 were given anoxic treatment in the dark using a glucose oxidase/catalase cocktail (State 2) [46].
277 For proteomic analyses of *STT7* experiments, TAP grown cells were shifted to State 2
278 conditions for 30 min and samples for phospho-proteomic analyses were collected. For ECS-
279 based state transition measurements, the cells (40 µg chlorophyll ml^{-1}) were bubbled with
280 argon gas for 15 min in the dark, followed by 1:1 dilution in TP-Ficol (20% *w/v*) and addition
281 of 20 µM DCMU. The strains were checked for photoautotrophic growth for two weeks by
282 spotting 20 µl of 3×10^5 cells/ml (and dilutions) on TP agar plates at 25°C kept under
283 continuous light at 40 and 200 µmol photons m^{-2} s^{-1}.
284

285 **Biochemical methods**

286 Liquid cultures of WT, T4A, T4E, and ΔN were grown in TAP medium and freshly diluted
287 one day before harvesting. The cells were pelleted and mixed in a buffer containing 0.2 M
288 dichloro-diphenyl-trichloroethane, 0.2 M Na_2CO_3, 10 mM NaF, and protease inhibitors (0.2
289 mM phenylmethylsulfonyl fluoride, 1 mM benzamidine, 20 mM amino caproic acid) to be
290 analyzed via SDS-PAGE [47]. For heme staining the b_6f was isolated using the standard
291 protocol [48] to analyze their purity via SDS-PAGE. The high-spin hemes were stained in gel
292 using 3,3',5,5'-tetramethylbenzidine [49]. Blue Native (BN) PAGE was carried out according to
293 the manufacturer's protocol (NativePAGE Bis-Tris; Thermo Fisher Scientific)
294

295 **Generation of *STT7* mutants with CRISPR-CAS9**

296 Chlamydomonas strain CC-125 (*nit1*; *nit2*; *mt+*) was grown in tris-acetate-phosphate (TAP)
297 media under continuous illumination of 50 µmol photons m^{-2} s^{-1} at 22 °C. Single guide RNAs
298 (sgRNAs) were designed by CHOPCHOP using version 5.6 of the *Chlamydomonas*
299 *reinhardtii* genome, and 5'-CTCCTGTAGACCGCTCAATGCGG was selected as the
300 targeting sequence, and sgRNAs were bought will all accessory parts to make it functional
301 (IDT, USA). Ribonucleic protein (RNP) complexes were prepared by duplexing the sgRNA

302 (23% volume per volume, v/v; IDT) and Cas-9 (19% v/v; IDT) within a duplex buffer (58%
303 v/v; IDT) and incubated at 37°C for 25 to 30 min. After treatment with autolysin for 3 hours
304 without shaking, cells were washed with TAP media supplemented with 40 mM of sucrose,
305 resuspended with the same supplemented media to approximately 2 x 10^8 cells mL^{-1}, and
306 electroporated in the presence of a hygromycin resistance DNA cassette (2 µg mL^{-1}) and the
307 37°C-incubated RNP mixture. After 10 min at room temperature, cells were resuspended in
308 10 mL of TAP media supplemented with 40 mM of sucrose and left without shaking
309 overnight in dim light (10-20 µmol photons m^{-2} s^{-1}) at 22°C. Hygromycin resistant
310 transformants were selected on solid TAP media (2% Agar w/v) containing hygromycin (20
311 µg mL^{-1}). sgRNA targeted regions were amplified via polymerase chain reaction (PCR) to
312 check for full or partial insertion of the hygromycin resistance cassette at the target site using
313 the following primers: STT7 F/R (for oligo sequences, see Extended data Table 1) with an
314 annealing temperature of 62.6°C (Extended Data Fig. 6). Impaired accumulation of the STT7
315 protein was then verified by immunodetection (Agrisera, AS15 3080).
316

317 **Sample preparation for mass spectrometry**

318 Protein isolation from cell pellets was carried out as described [43]. Reduction/alkylation of
319 cysteines and tryptic digestion of proteins (100 µg per sample) was performed following the
320 SP4 protocol [50] . After digestion, peptides were desalted using PurePep H50 SPE Spin
321 columns (Affinisep). The peptide samples were divided into two aliquots: 5 µg for whole
322 proteome analysis and 95 µg for phosphopeptide enrichment. Both aliquots were dried using
323 vacuum centrifugation before further processing.

324 To enrich phosphopeptides, titanium dioxide (TiO2) beads with 5 µm particle size
325 (Titansphere, GL Sciences) in a metal oxide affinity chromatography (MOAC) procedure
326 were used. TiO2 (1 mg per sample) was activated once with acetonitrile and equilibrated three
327 times with loading buffer (LB; 80% (v/v) acetonitrile/5% (v/v) TFA/1 M glycolic acid).
328 Loading buffer was added to create a 10% (w/v) TiO2 suspension. Peptide samples were
329 dissolved in 50 µl LB, combined with 10 µl TiO2 suspension, and incubated for 30 minutes at
330 25°C in an Eppendorf Thermomixer at 1,200 rpm). The mixture was transferred to SDB-XC
331 STAGE tips prepared in-house [51]. Unless stated otherwise, all subsequent washing and elution
332 steps were performed using 60 µl buffer volumes with in-between centrifugation at 2000 × g
333 at room temperature. The buffer was removed by centrifugation and the TiO2 beads were
334 washed twice with LB and once with 1% (v/v) acetonitrile/0.1% (v/v) TFA (W1). Non-
335 phosphorylated peptides that were removed from the beads and subsequently bound to the
336 SDB-XC membrane plug were removed by one wash with 80% (v/v) acetonitrile/0.1% (v/v)
337 TFA (W2). The phosphopeptides were eluted from the TiO2 beads onto the SDB-XC material
338 using 160 µl of pH 11 buffer (0.4 M sodium hydrogen phosphate/NaOH with 1%
339 acetonitrile). After washing once with 1% acetonitrile/0.1% TFA, the phosphopeptides were
340 sequentially eluted in three fractions using increasing concentrations of acetonitrile (7.5%,

341 20%, and 60%) in 100 mM ammonium formate (pH10). For samples from the STT7
342 experiment, only one fraction (60% acetonitrile in 100 mM ammonium formate (pH10)) was
343 collected. The strongly bound phosphopeptides were eluted in two steps: first from the TiO2
344 beads using 5% ammonia, then from the SDB-CX membrane using 60% acetonitrile in 100
345 mM ammonium formate at pH 10. All fractions were dried by vacuum centrifugation and
346 stored at -80°C until MS analysis.
347
348 **Mass spectrometry**
349 Whole proteome analysis
350 Dried peptide samples were reconstituted in 5 µl of 2% (v/v) acetonitrile/0.05% (v/v) TFA in
351 LC/MS grade water. Samples were analyzed on an LC-MS/MS system consisting of an
352 Ultimate 3000 NanoLC (Thermo Fisher Scientific) coupled via a Nanospray Flex ion source
353 (Thermo Fisher Scientific) to a Q Exactive Plus mass spectrometer (Thermo Fisher
354 Scientific). Peptides were concentrated on a trap column (Acclaim Pepmap C18, 5 × 0.3 mm,
355 3 µm particle size, Thermo Scientific) for 3 min using 4% (v/v) acetonitrile/0.05% (v/v) in
356 LC/MS grade water at a flow rate of 10 µl/min. The trap column was operated in back-flush
357 mode, allowing the transfer of peptides on a reversed-phase column (PepSep Fifty, 500 ×
358 0.075 mm, 1.9 µm particle size, Bruker) for chromatographic separation. The eluents used
359 were 0.1% (v/v) formic acid in LC/MS grade water (A) and 0.1% (v/v) formic acid/80% (v/v)
360 acetonitrile in LC/MS grade water (B). The gradient was programmed as follows: 2.5% to 5%
361 B over 5 min, 5% to 17.5% B over 47 min, 17.5% to 40% B over 105 min, 40% to 99% B
362 over 10 min, and 99% B for 20 min. Flow rate was 250 nl/min. The mass spectrometer was
363 operated in data-dependent acquisition (DDA) mod, alternating between one MS1 full scan
364 and up to 12 MS2 scans. Full scans were acquired with the following settings: AGC target
365 3e6, MS1 resolution 70000, maximum injection time 50 ms, scan range: 350–1400 m/z.
366 Settings for MS were: AGC target 5e4, resolution 17500, MS2 maximum injection time 80
367 ms, intensity threshold 1e4, normalized collision energy 27 (HCD)). Dynamic exclusion was
368 set to 'auto', assuming a chromatographic peak width (FWHM) of 60 s.
369
370 **Phosphoproteomic analysis**
371 Prior to analysis, dried peptide samples were reconstituted in 5 µl of 2% (v/v)
372 acetonitrile/0.05% (v/v) TFA in LC/MS grade water. LC-MS/MS system, flow rate and eluent
373 compositions were the same as described above. The gradient for peptide separation was as
374 follows: 2.5% to 5% B over 5 min, 5% to 40% B over 92 min, 40% to 99% B over 10 min,
375 and 99% B for 20 min.
376 The mass spectrometer used the same DDA mode settings as the whole proteome analysis,
377 with two changes: MS2 maximum injection time was increased to 120 ms, and dynamic
378 exclusion was set to 45 s.

379

380 **MS data analysis**

381 For quantitative phosphoproteome analysis of four biological replicates, mass spectrometry
382 raw data from nonenriched and enriched samples were searched using Fragpipe [52,53] against a
383 concatenated, non-redundant database containing *Chlamydomonas reinhardtii* protein
384 sequences from v5.6 and v6.1 gene models (Phytozome 13, phytozome-next.jgi.doe.gov). In
385 addition, the polypeptide sequences of mutated/tagged proteins were added to the database.
386 Default 'LFQ-MBR' workflow settings were applied to data from whole proteome samples,
387 while the 'LFQ-phospho' workflow was used for phosphopeptide samples. A false discovery
388 rate of 1% was applied at both peptide and protein levels.

389 Fragpipe output files containing peptide/protein identifications and quantitative data
390 ('combined_modified_peptide.tsv' from enriched samples and 'combined_protein.tsv' from
391 whole proteome samples) were reformatted using a custom Python script to ensure
392 compatibility with Phospho-Analyst (v. 1.0.2), which was used for differential expression
393 analysis [54]: Missing values were imputed using the 'MinProb' function, and variance
394 stabilizing transformation was applied to normalize phosphosite intensities. Since the whole
395 proteome LFQ data was already normalized in Fragpipe, no additional normalization steps
396 were needed. Phospho-Analyst automatically corrected phosphosite abundance changes for
397 underlying protein levels. A phosphorylation site localization probability threshold of 0.33
398 was applied, and p-values were adjusted using the Benjamini-Hochberg method. Predicted
399 protein localizations are based on recently published data (PB-Chlamy)[55].

400

401 **Optical spectroscopy**

402 The flash-induced b_6f measurements were carried out by using a Joliot-type
403 spectrophotometer (JTS-150, SpectroLogiX) equipped with the interference filters and
404 deconvolution procedures as reported previously [3]. Cells were adapted to alternating 7.5 s
405 darkness and 5 s actinic light (AL; 550 µmol photons m^{-2} s^{-1} peaking at 630 nm). Sub-
406 saturating 6-ns flashes (Q-switched Nd:YAG, Continuum) were fired at 3 s darkness, hitting
407 ~40% of PSI. Three averaged baseline spectra (in the absence of a flash) were subtracted from
408 each flash measurement at the b_6f-specific wavelengths. For multiple turnover conditions,
409 previously described conditions and protocols used cells which were adapted to alternating
410 2.5 s AL and dark. Briefly, ETR were obtained in the presence of LEF but referred to PSI
411 charge separation activity. This stems from separate ECS calibration measurements that
412 allowed, via saturating single-turnover flashes, for the conversion of optical changes
413 (obtained as $\Delta I/I$ at 520 nm - 546nm) into the ECS signals corresponding to 1 PSI charge
414 separation [56]. The ETR protocol was based on a Dark Interval Relaxation Kinetics approach
415 [57,58]. P700 measurements relied on the Klughammer & Schreiber method [59]. The ECS-based
416 state transition method is described elsewhere [26]; it measures PSI-driven charge separation

rates as a function of PSI antenna size. Accordingly, the extent of State 2 to State 1 transition under light and DCMU displayed as a flattening of ECS slopes acquired during a 20-min measurement sequence (AL as above, 10 µM DCMU; Figures 1e–g). The kinetics were fitted using the exponential decay function $y = y_0 + Ae^{-(x-x_0)/t_1}$. The state transition extent was expressed as $(A + y_0)/y_0$, where y_0 is the y-offset and A the amplitude. For fitting, the x-offset x_0 was fixed at 10 s, corresponding to the minimal pre-illumination period of the State 2 reference sample.

Data availability statement

All data supporting the findings of this study are available within the paper and its Supplementary Information. The mass spectrometry proteomics data have been deposited to the ProteomeXchange Consortium (proteomecentral.proteomexchange.org) via the PRIDE partner repository [60] with the dataset identifier PXD060640. The generated mutant cell lines are available on request from authors. The *STT7* mutant is available in the Chlamydomonas Resource Center (CC-6272; www.chlamycollection.org).

References

1 Malone, L. A., Proctor, M. S., Hitchcock, A., Hunter, C. N. & Johnson, M. P. Cytochrome b(6)f - Orchestrator of photosynthetic electron transfer. *Biochim Biophys Acta Bioenerg* **1862**, 148380, doi:10.1016/j.bbabio.2021.148380 (2021).

2 Mitchell, P. The protonmotive Q cycle: a general formulation. *FEBS Lett* **59**, 137-139, doi:10.1016/0014-5793(75)80359-0 (1975).

3 Buchert, F., Mosebach, L., Gabelein, P. & Hippler, M. PGR5 is required for efficient Q cycle in the cytochrome b6f complex during cyclic electron flow. *Biochem J* **477**, 1631-1650, doi:10.1042/BCJ20190914 (2020).

4 Rumberg, B. & Siggel, U. Ph Changes in Inner Phase of Thylakoids during Photosynthesis. *Naturwissenschaften* **56**, 130-+, doi:Doi 10.1007/Bf00601025 (1969).

5 Nishio, J. N. & Whitmarsh, J. Dissipation of the Proton Electrochemical Potential in Intact Chloroplasts (II. The pH Gradient Monitored by Cytochrome f Reduction Kinetics). *Plant Physiol* **101**, 89-96, doi:10.1104/pp.101.1.89 (1993).

6 Li, X. P. *et al.* A pigment-binding protein essential for regulation of photosynthetic light harvesting. *Nature* **403**, 391-395 (2000).

7 Peers, G. *et al.* An ancient light-harvesting protein is critical for the regulation of algal photosynthesis. *Nature* **462**, 518-521, doi:10.1038/nature08587 (2009).

8 Girolomoni, L. *et al.* LHCSR3 is a nonphotochemical quencher of both photosystems in. *P Natl Acad Sci USA* **116**, 4212-4217, doi:10.1073/pnas.1809812116 (2019).

9 Allorent, G. *et al.* A dual strategy to cope with high light in Chlamydomonas reinhardtii. *Plant Cell* **25**, 545-557, doi:10.1105/tpc.112.108274 (2013).

10 Depege, N., Bellafiore, S. & Rochaix, J. D. Role of chloroplast protein kinase Stt7 in LHCII phosphorylation and state transition in Chlamydomonas. *Science* **299**, 1572-1575, doi:10.1126/science.1081397 (2003).

11 Rochaix, J. D. Regulation and dynamics of the light-harvesting system. *Annu Rev Plant Biol* **65**, 287-309, doi:10.1146/annurev-arplant-050213-040226 (2014).
12 Cariti, F. *et al.* Regulation of Light Harvesting in Chlamydomonas reinhardtii Two Protein Phosphatases Are Involved in State Transitions. *Plant Physiol* **183**, 1749-1764, doi:10.1104/pp.20.00384 (2020).
13 Lemeille, S. *et al.* Analysis of the chloroplast protein kinase Stt7 during state transitions. *PLoS Biol* **7**, e45, doi:10.1371/journal.pbio.1000045 (2009).
14 Shapiguzov, A. *et al.* Activation of the Stt7/STN7 Kinase through Dynamic Interactions with the Cytochrome b_6f Complex. *Plant Physiol* **171**, 82-92, doi:10.1104/pp.15.01893 (2016).
15 Singh, S. K. *et al.* Trans-membrane signaling in photosynthetic state transitions: Redox- and structure-dependent interaction *in vitro* between STT7 kinase and the cytochrome b_6f complex. *J Biol Chem* **291**, 21740-21750, doi:10.1074/jbc.M116.732545 (2016).
16 Wu, J. *et al.* Functional redox links between Lumen Thiol Oxidoreductase1 and Serine/Threonine-protein kinase STN7. *Plant Physiol*, doi:10.1093/plphys/kiab091 (2021).
17 Dumas, L. *et al.* A stromal region of cytochrome b_6f subunit IV is involved in the activation of the Stt7 kinase in *Chlamydomonas*. *Proc Natl Acad Sci U S A* **114**, 12063-12068, doi:10.1073/pnas.1713343114 (2017).
18 Riche, A. *et al.* The stromal side of the cytochrome b6f complex regulates state transitions. *Plant Cell* **36**, 4234-4244, doi:10.1093/plcell/koae190 (2024).
19 Bergner, S. V. *et al.* STATE TRANSITION7-dependent phosphorylation is modulated by changing environmental conditions, and its absence triggers remodeling of photosynthetic protein complexes. *Plant Physiol* **168**, 615-634, doi:10.1104/pp.15.00072 (2015).
20 McConnell, E. W., Werth, E. G. & Hicks, L. M. The phosphorylated redox proteome of Chlamydomonas reinhardtii: Revealing novel means for regulation of protein structure and function. *Redox Biol* **17**, 35-46, doi:10.1016/j.redox.2018.04.003 (2018).
21 Choquet, Y., Zito, F., Wostrikoff, K. & Wollman, F. A. Cytochrome *f* translation in *Chlamydomonas* chloroplast is autoregulated by its carboxyl-terminal domain. *Plant Cell* **15**, 1443-1454 (2003).
22 Takahashi, H. *et al.* PETO Interacts with Other Effectors of Cyclic Electron Flow in *Chlamydomonas*. *Mol Plant* **9**, 558-568, doi:10.1016/j.molp.2015.12.017 (2016).
23 Dinc, E. *et al.* LHCSR1 induces a fast and reversible pH-dependent fluorescence quenching in LHCII in Chlamydomonas reinhardtii cells. *Proc Natl Acad Sci U S A* **113**, 7673-7678, doi:10.1073/pnas.1605380113 (2016).
24 Wollman, F.-A. & Lemaire, C. Studies on kinase-controlled state transitions in Photosystem II and b_6f mutants from *Chlamydomonas reinhardtii* which lack quinone-binding proteins. *Biochimica et Biophysica Acta (BBA) - Bioenergetics* **933**, 85-94, doi:https://doi.org/10.1016/0005-2728(88)90058-8 (1988).
25 Wollman, F.-A. & Bennoun, P. A new chlorophyll-protein complex related to Photosystem I in *Chlamydomonas reinhardtii*. *Biochim Biophys Acta* **680**, 352-360 (1982).
26 Takahashi, H., Clowez, S., Wollman, F. A., Vallon, O. & Rappaport, F. Cyclic electron flow is redox-controlled but independent of state transition. *Nat Commun* **4**, 1954, doi:10.1038/ncomms2954 (2013).
27 Nawrocki, W. J., Santabarbara, S., Mosebach, L., Wollman, F. A. & Rappaport, F. State transitions redistribute rather than dissipate energy between the two photosystems in Chlamydomonas. *Nature Plants* **2**, doi:Artn 16031 10.1038/Nplants.2016.31 (2016).

28 Scholz, M. *et al.* Light-dependent N-terminal phosphorylation of LHCSR3 and LHCB4 are interlinked in *Chlamydomonas reinhardtii*. *Plant J* **99**, 877-894, doi:10.1111/tpj.14368 (2019).
29 Lemeille, S., Turkina, M. V., Vener, A. V. & Rochaix, J. D. Stt7-dependent phosphorylation during state transitions in the green alga Chlamydomonas reinhardtii. *Molecular & cellular proteomics : MCP* **9**, 1281-1295, doi:10.1074/mcp.M000020-MCP201 (2010).
30 Pan, X. *et al.* Structural basis of LhcbM5-mediated state transitions in green algae. *Nat Plants* **7**, 1119-1131, doi:10.1038/s41477-021-00960-8 (2021).
31 Buchert, F. *et al.* The labile interactions of cyclic electron flow effector proteins. *J Biol Chem* **293**, 17559-17573, doi:10.1074/jbc.RA118.004475 (2018).
32 Pfalz, J., Liere, K., Kandlbinder, A., Dietz, K. J. & Oelmuller, R. pTAC2, -6, and -12 are components of the transcriptionally active plastid chromosome that are required for plastid gene expression. *Plant Cell* **18**, 176-197, doi:10.1105/tpc.105.036392 (2006).
33 Ingelsson, B. & Vener, A. V. Phosphoproteomics of Arabidopsis chloroplasts reveals involvement of the STN7 kinase in phosphorylation of nucleoid protein pTAC16. *FEBS Lett* **586**, 1265-1271, doi:10.1016/j.febslet.2012.03.061 (2012).
34 Alric, J., Pierre, Y., Picot, D., Lavergne, J. & Rappaport, F. Spectral and redox characterization of the heme c_i of the cytochrome b_6f complex. *Proc Natl Acad Sci U S A* **102**, 15860-15865, doi:10.1073/pnas.0508102102 (2005).
35 Buchert, F., Scholz, M. & Hippler, M. Electron transfer via cytochrome b_6f complex displays sensitivity to antimycin A upon STT7 kinase activation. *Biochem J* **479**, 111-127, doi:10.1042/BCJ20210802 (2022).
36 Valkova-Valchanova, M., Darrouzet, E., Moomaw, C. R., Slaughter, C. A. & Daldal, F. Proteolytic Cleavage of the Fe−S Subunit Hinge Region of Rhodobacter capsulatus bc1 Complex: Effects of Inhibitors and Mutations. *Biochemistry* **39**, 15484-15492, doi:10.1021/bi000751d (2000).
37 Cooley, J. W., Lee, D.-W. & Daldal, F. Across Membrane Communication between the Qo and Qi Active Sites of Cytochrome bc1. *Biochemistry* **48**, 1888-1899, doi:10.1021/bi802216h (2009).
38 Pintscher, S. *et al.* Molecular basis of plastoquinone reduction in plant cytochrome b(6)f. *Nat Plants*, doi:10.1038/s41477-024-01804-x (2024).
39 Zito, F. *et al.* The Qo site of cytochrome b_6f complexes controls the activation of the LHCII kinase. *EMBO J* **18**, 2961-2969, doi:10.1093/emboj/18.11.2961 (1999).
40 Calzadilla, P. I. & Kirilovsky, D. Revisiting cyanobacterial state transitions. *Photochem Photobiol Sci* **19**, 585-603, doi:10.1039/c9pp00451c (2020).
41 Lepetit, B. *et al.* in *The Molecular Life of Diatoms* (eds Angela Falciatore & Thomas Mock) 423-464 (Springer International Publishing, 2022).
42 Mekala, N. R., Suorsa, M., Rantala, M., Aro, E. M. & Tikkanen, M. Plants Actively Avoid State Transitions upon Changes in Light Intensity: Role of Light-Harvesting Complex II Protein Dephosphorylation in High Light. *Plant physiology* **168**, 721-734, doi:10.1104/pp.15.00488 (2015).
43 Younas, M., Scholz, M., Marchetti, G. M. & Hippler, M. Remodeling of algal photosystem I through phosphorylation. *Biosci Rep* **43**, doi:10.1042/BSR20220369 (2023).
44 Fu, H. Y. *et al.* Redesigning the Q(A) binding site of Photosystem II allows reduction of exogenous quinones. *Nat Commun* **8**, 15274, doi:10.1038/ncomms15274 (2017).
45 Gorman, D. S. & Levine, R. P. Cytochrome *f* and plastocyanin: their sequence in the photosynthetic electron transport chain of *Chlamydomonas reinhardtii*. *Proc Natl Acad Sci U S A* **54**, 1665-1669 (1965).

46 Buchert, F., Mosebach, L., Gäbelein, P. & Hippler, M. PGR5 is required for efficient Q cycle in the cytochrome b_6f complex during cyclic electron flow. *Biochemical Journal* **477**, 1631-1650, doi:10.1042/bcj20190914 (2020).

47 Schägger, H. & Von Jagow, G. Tricine-sodium dodecyl sulfate-polyacrylamide gel electrophoresis for the separation of proteins in the range from 1 to 100 kDa. *Analytical biochemistry* **166**, 368-379 (1987).

48 Stroebel, D., Choquet, Y., Popot, J. L. & Picot, D. An atypical haem in the cytochrome b_6f complex. *Nature* **426**, 413-418, doi:10.1038/nature02155 (2003).

49 Thomas, P. E., Ryan, D. & Levin, W. An improved staining procedure for the detection of the peroxidase activity of cytochrome P-450 on sodium dodecyl sulfate polyacrylamide gels. *Anal Biochem* **75**, 168-176, doi:10.1016/0003-2697(76)90067-1 (1976).

50 Johnston, H. E. *et al.* Solvent Precipitation SP3 (SP4) Enhances Recovery for Proteomics Sample Preparation without Magnetic Beads. *Anal Chem* **94**, 10320-10328, doi:10.1021/acs.analchem.1c04200 (2022).

51 Rappsilber, J., Mann, M. & Ishihama, Y. Protocol for micro-purification, enrichment, pre-fractionation and storage of peptides for proteomics using StageTips. *Nature Protocols* **2**, 1896-1906, doi:10.1038/nprot.2007.261 (2007).

52 Kong, A. T., Leprevost, F. V., Avtonomov, D. M., Mellacheruvu, D. & Nesvizhskii, A. I. MSFragger: ultrafast and comprehensive peptide identification in mass spectrometry–based proteomics. *Nature Methods* **14**, 513-520, doi:10.1038/nmeth.4256 (2017).

53 Yu, F. *et al.* Analysis of DIA proteomics data using MSFragger-DIA and FragPipe computational platform. *Nat Commun* **14**, 4154, doi:10.1038/s41467-023-39869-5 (2023).

54 Zhang, H. *et al.* Phospho-Analyst: An Interactive, Easy-to-Use Web Platform To Analyze Quantitative Phosphoproteomics Data. *J Proteome Res* **22**, 2890-2899, doi:10.1021/acs.jproteome.3c00186 (2023).

55 Wang, L. *et al.* A chloroplast protein atlas reveals punctate structures and spatial organization of biosynthetic pathways. *Cell* **186**, 3499-3518.e3414, doi:https://doi.org/10.1016/j.cell.2023.06.008 (2023).

56 Bailleul, B., Cardol, P., Breyton, C. & Finazzi, G. Electrochromism: a useful probe to study algal photosynthesis. *Photosynthesis Research* **106**, 179-189, doi:10.1007/s11120-010-9579-z (2010).

57 Sacksteder, C. A. & Kramer, D. M. Dark-interval relaxation kinetics (DIRK) of absorbance changes as a quantitative probe of steady-state electron transfer. *Photosynth Res* **66**, 145, doi:10.1023/a:1010785912271 (2000).

58 Joliot, P. & Joliot, A. Cyclic electron transfer in plant leaf. *Proc Natl Acad Sci U S A* **99**, 10209-10214, doi:10.1073/pnas.102306999 (2002).

59 Klughammer, C. & Schreiber, U. An improved method, using saturating light-pulses, for the determination of photosystem-I quantum yield via $P700^+$-absorbance changes at 830nm. *Planta* **192**, 261-268 (1994).

60 Perez-Riverol, Y. *et al.* The PRIDE database and related tools and resources in 2019: improving support for quantification data. *Nucleic acids research* **47**, D442-D450 (2019).

Acknowledgements

M.H. (507704013) and F. B. (507704013) acknowledge funding by the Deutsche Forschungsgemeinschaft (DFG FOR 5573/1). M.H. acknowledges the RECTOR program in association with the University of Okayama, Japan. F. B. acknowledges Deutsche Forschungsgemeinschaft 461765884. Y.M. acknowledges the Alexander von Humboldt Foundation for a Research Fellowship for postdocs (1219125). A.B. acknowledges the support of Carnegie Science. The authors thank Sai Kiran Madireddi for helping with the initial production and characterisation of the *STT7* mutant.

Author contributions

M.H. and F.B. designed the project. A.Z. and F.B. did genetic engineering and kinetic measurements and analyses. S.B. contributed to mutant analyses. C.S. and A.B. produced the *STT7* KO strains. M.S. did the mass spectrometric measurements and data evaluation. M.S. and M.H. analysed the mass spectrometric data. M.H wrote the manuscript with contributions from F.B., A.Z., A.B. and M.S. All authors contributed to the analysis and the final version of the manuscript.

Competing interests

The authors declare no competing interests.

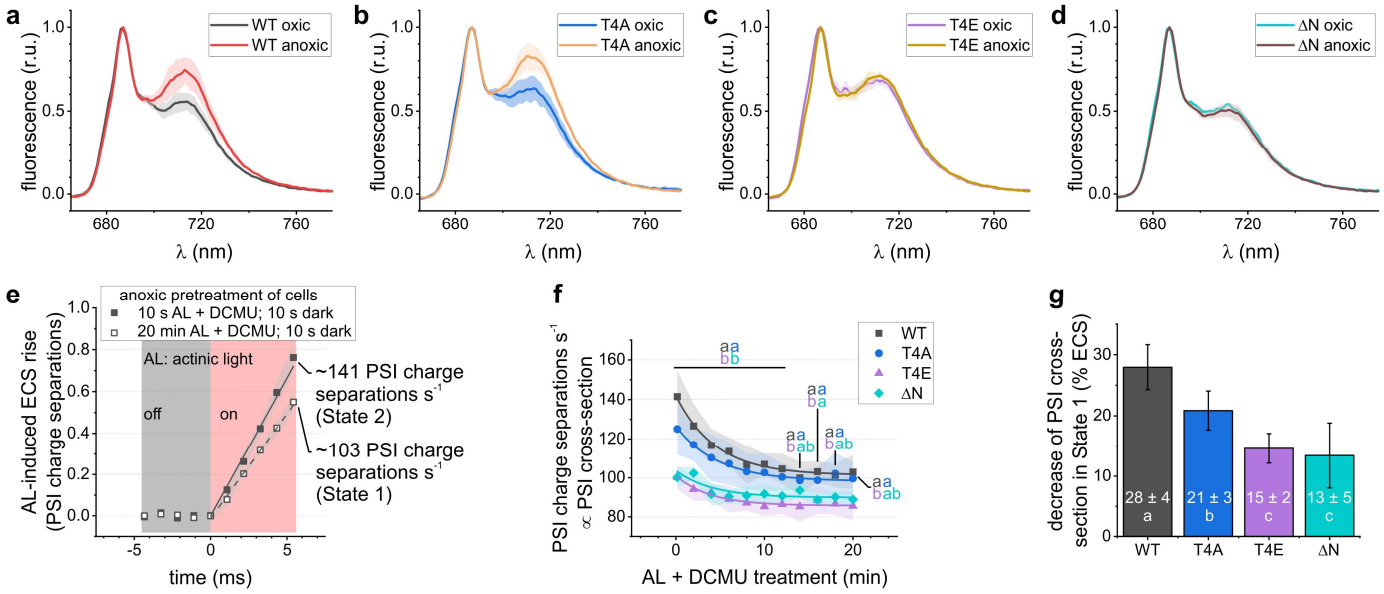

Fig. 1. The relative antenna cross section is shown by measuring chlorophyll fluorescence emission spectra at 77 K and electrochromism. Panels **a** – **d** highlight the differences in antenna attached to photosystem (PS) I under State 1 (oxic) and State 2 (anoxic), contributing to ~712 nm emissions. These spectra were averaged and normalized to PSII-attached antenna emission signals at ~687 nm (biological replicates $N = 3 \pm$ SD). **e** The electrochromic shift (ECS) rise was recorded in DCMU-treated anaerobic cells during light-driven PQ pool oxidation. Traces were normalized to PSI. **f** The initial ECS slope decreased with reduction in PSI antenna size after state transition treatments. **g** The fitted amplitude from panel f was put in relation to the y-offset to calculate the extent of state transitions ($N = 4 \pm$ SD; letters indicate statistical significances via One-Way ANOVA/Fisher-LSD, $P < 0.05$).

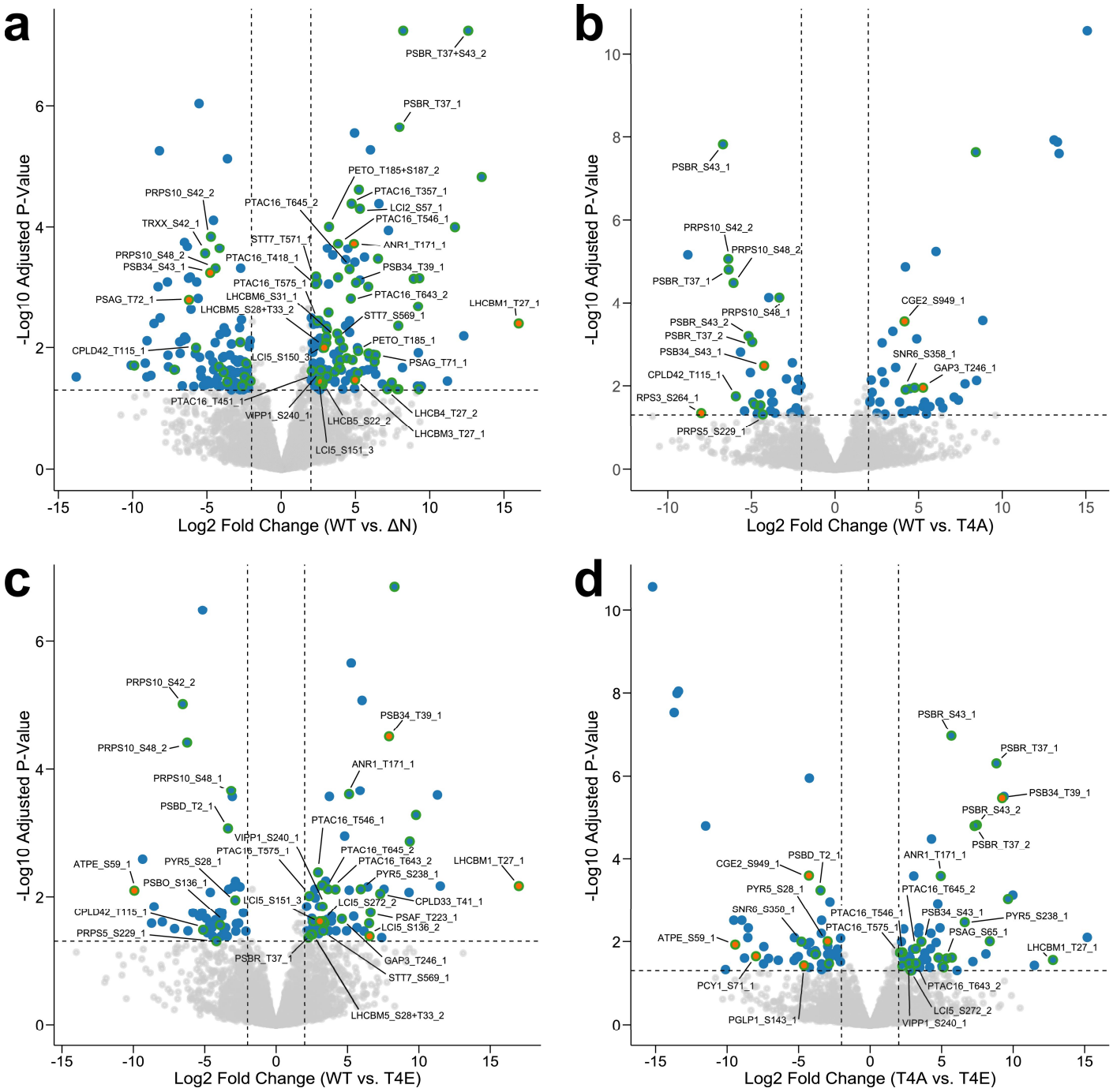

Fig. 2. Volcano plots visualizing effect of PetD mutations on protein phosphorylation. Phosphorylation sites with FDR-adjusted p-value < 0.05 and $|\log_2$ fold change$|$ > 2 are highlighted in blue, with threshold boundaries shown as dashed lines. Data points are shown in orange instead of blue when all values for one strain in the fold-change calculation are imputed due to completely missing data. Green halos indicate chloroplast-encoded proteins and nuclear-encoded proteins with confirmed or predicted (PB-Chlamy) chloroplast localization. Phosphorylation $\log_2$ fold changes are normalized to corresponding protein abundance levels to account for changes in protein expression. Numbers at the end of data labels indicate peptide multiplicity (total phosphorylations per peptide, e.g. PRPS10_S42_2 = PRPS10 with phosphorylated S42 and one additional phosphorylation on the same peptide). Comparisons are shown for **a** WT vs. ΔN, **b** WT vs. T4A, **c** WT vs. T4E, and **d** T4A vs. T4E.

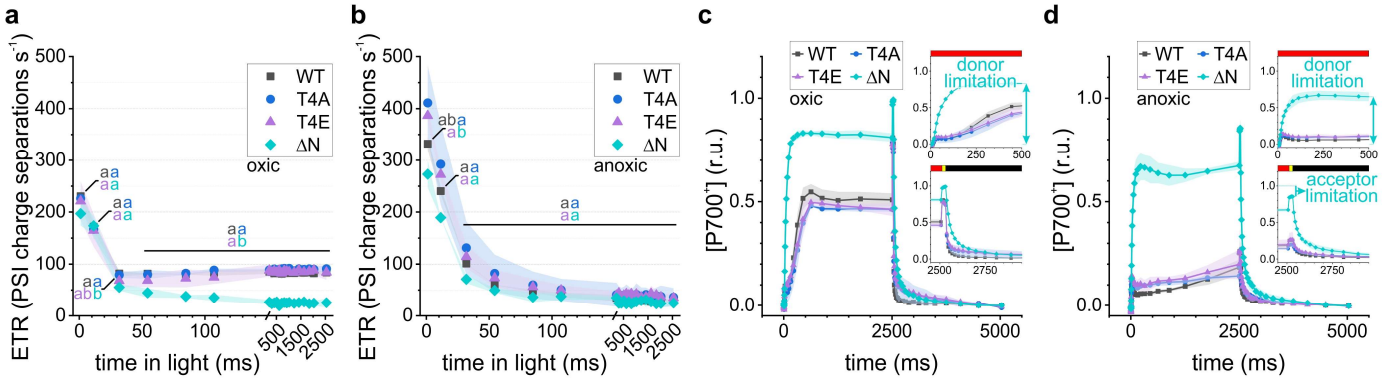

Fig. 3. Photosynthetic activities of the cytochrome *b*$_6$*f* variants are shown. Averaged kinetics are depicted (biological replicates $N = 3 \pm$ SD). **a**, Electron transfer rates (ETR) developed over the 2.5-s illumination period under oxic conditions, with the first detection at 1-ms of actinic light. The letters at the punctual rates indicate statistical significances (One-Way ANOVA/Tukey-HSD, $P < 0.05$) **b**, ETR developments are shown under anoxic conditions. **c**, Quantification of oxidized primary PSI donor ([P700$^+$]) is plotted under oxic conditions. Red, yellow, and black bar represent actinic light intensities of 550, 3000, and 0 µmol photons m^{-2} s^{-1}. **d**, The P700 kinetics are shown as in panel c but under anoxic conditions.

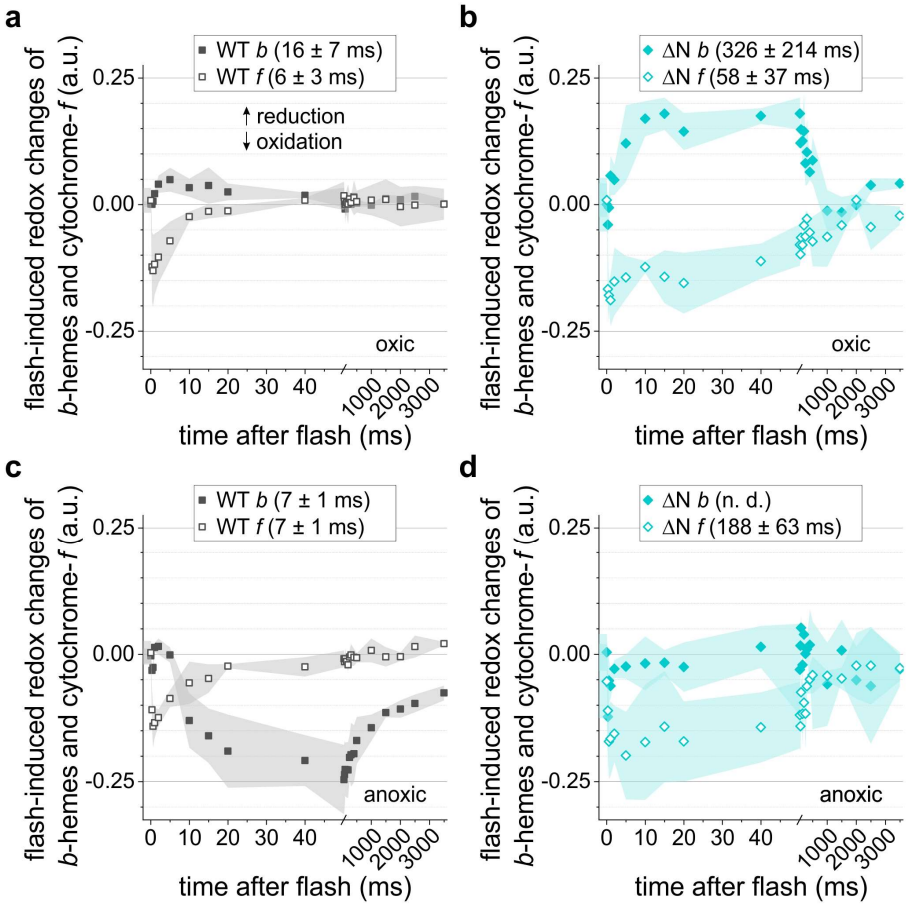

Fig. 4. Single turnover redox changes of the cytochrome b_6f hemes are shown. Averaged kinetics are depicted (biological replicates $N = 3 \pm$ SD). WT (**a**, **c**) as well as the ΔN mutant (**b**, **d**) were measured under oxic (**a**, **b**) and anoxic conditions (**c**, **d**). The averaged half-times of cytochrome-*f* reduction and *b*-hemes oxidation are given in the panels' legends (n. d.; not determined).

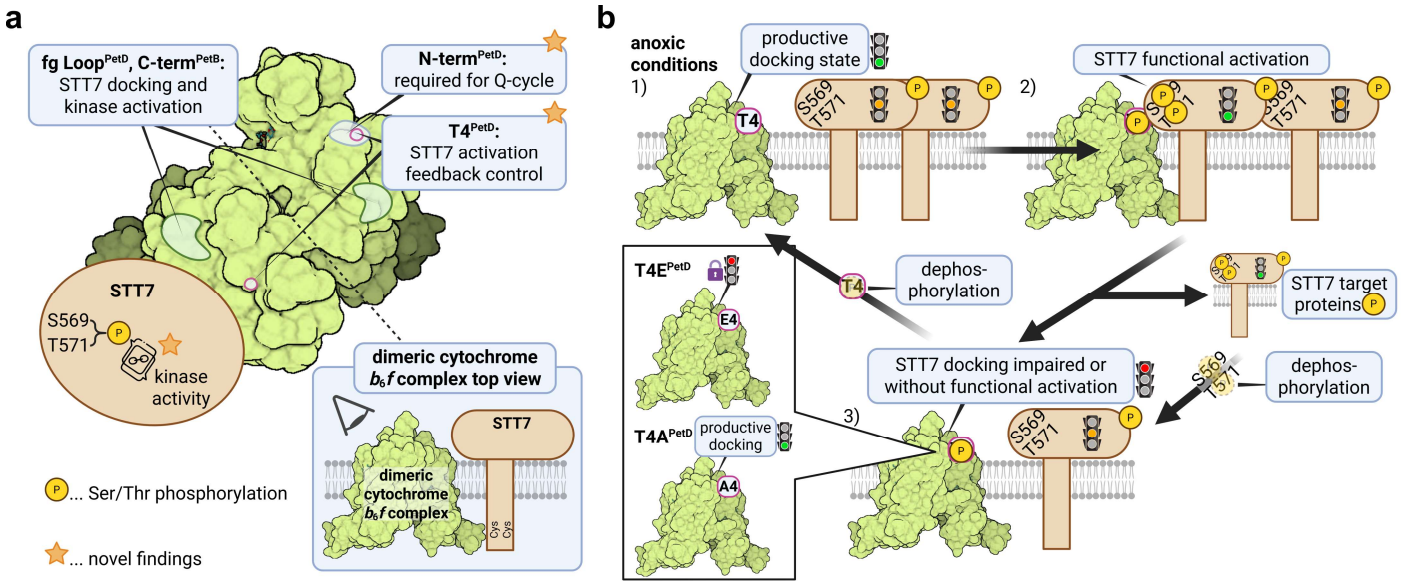

Extended Data Fig. 1. Graphical abstract of the cytochrome *b*$_6$*f* complex interplay with STT7 kinase regulation. a, The N-terminus of PetD has been investigated and the focus was on T4. The model is built on previous STT7 docking studies (references 17 and 18 in the main text) and disregards possible STT7 oligomerization and redox regulation for the sake of simplicity. **b**, The feedback loop upon PetD T4 phosphorylation as well as investigated mutants is summarized. The figure was created with Biorender.

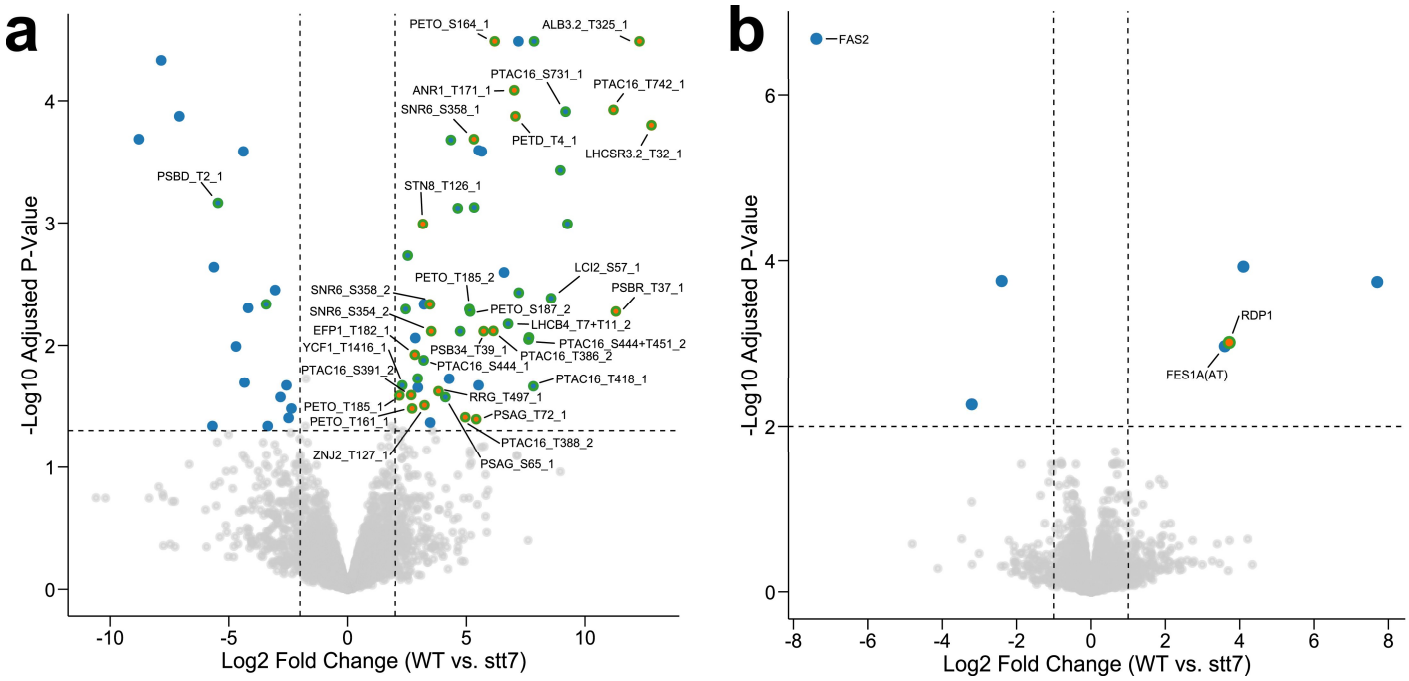

Extended Data Fig. 2. Volcano plots visualizing differential phosphorylation (a) and protein expression (b) between WT and *STT7* mutant. Proteins with FDR-adjusted p-value < 0.01 and $|\log_2$ fold change$| > 1$ are highlighted in blue, with threshold boundaries shown as dashed lines. Data points are shown in orange instead of blue when all values for one strain in the fold-change calculation are imputed due to completely missing data. Green halos indicate chloroplast-encoded proteins and nuclear-encoded proteins with confirmed or predicted (PB-Chlamy) chloroplast localization.

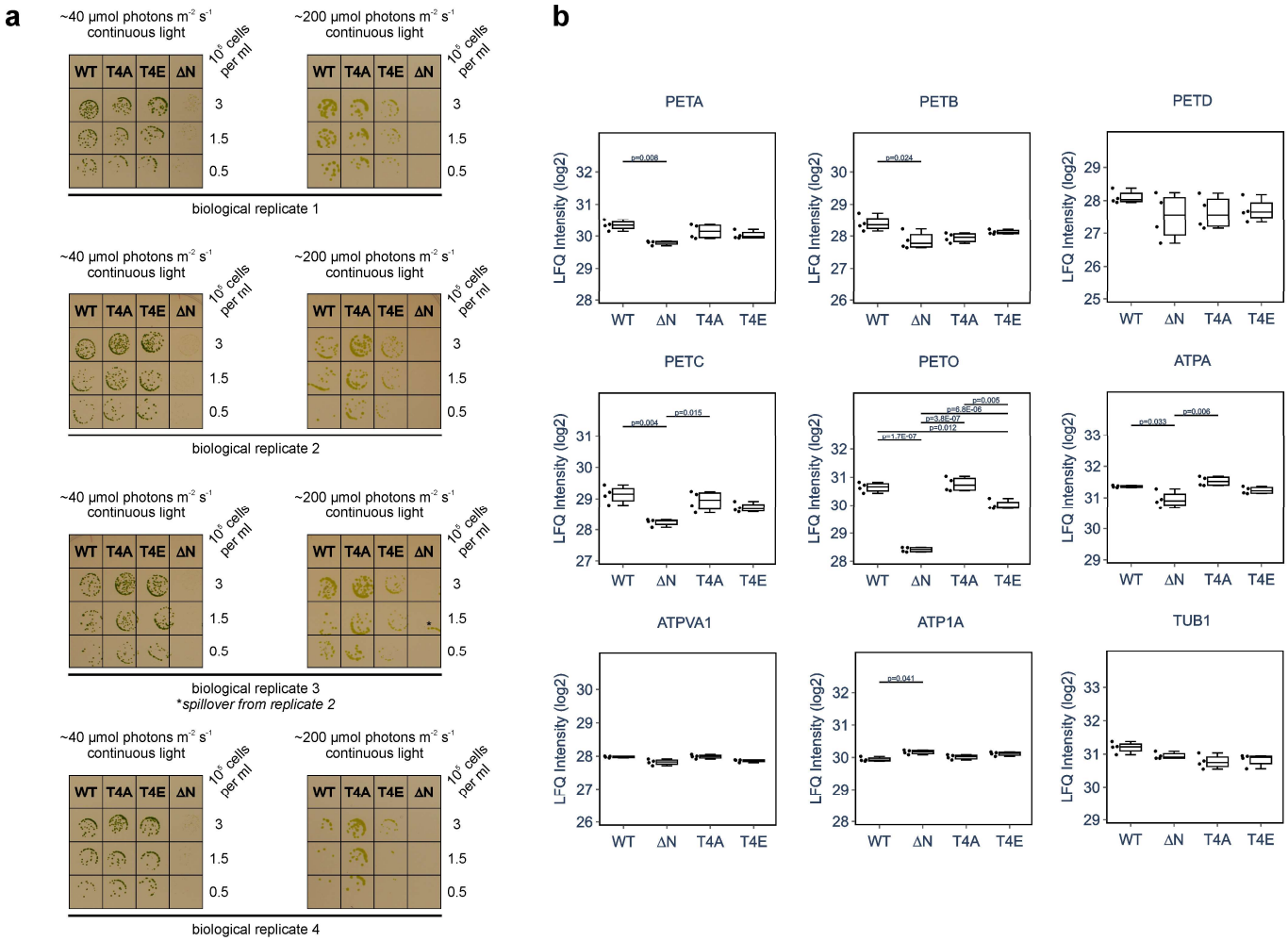

Extended Data Fig. 3. Growth analysis in varying light conditions and protein expression in the mutants. **a**. Spot tests on minimal media compare the growth under two light conditions (40 and 200 µmol photons m^{-2} s^{-1}). **b**. Protein expression of *b_6f* subunits and control proteins in the engineered PetD strains. The box plots visualize the log_2 protein LFQ intensities.

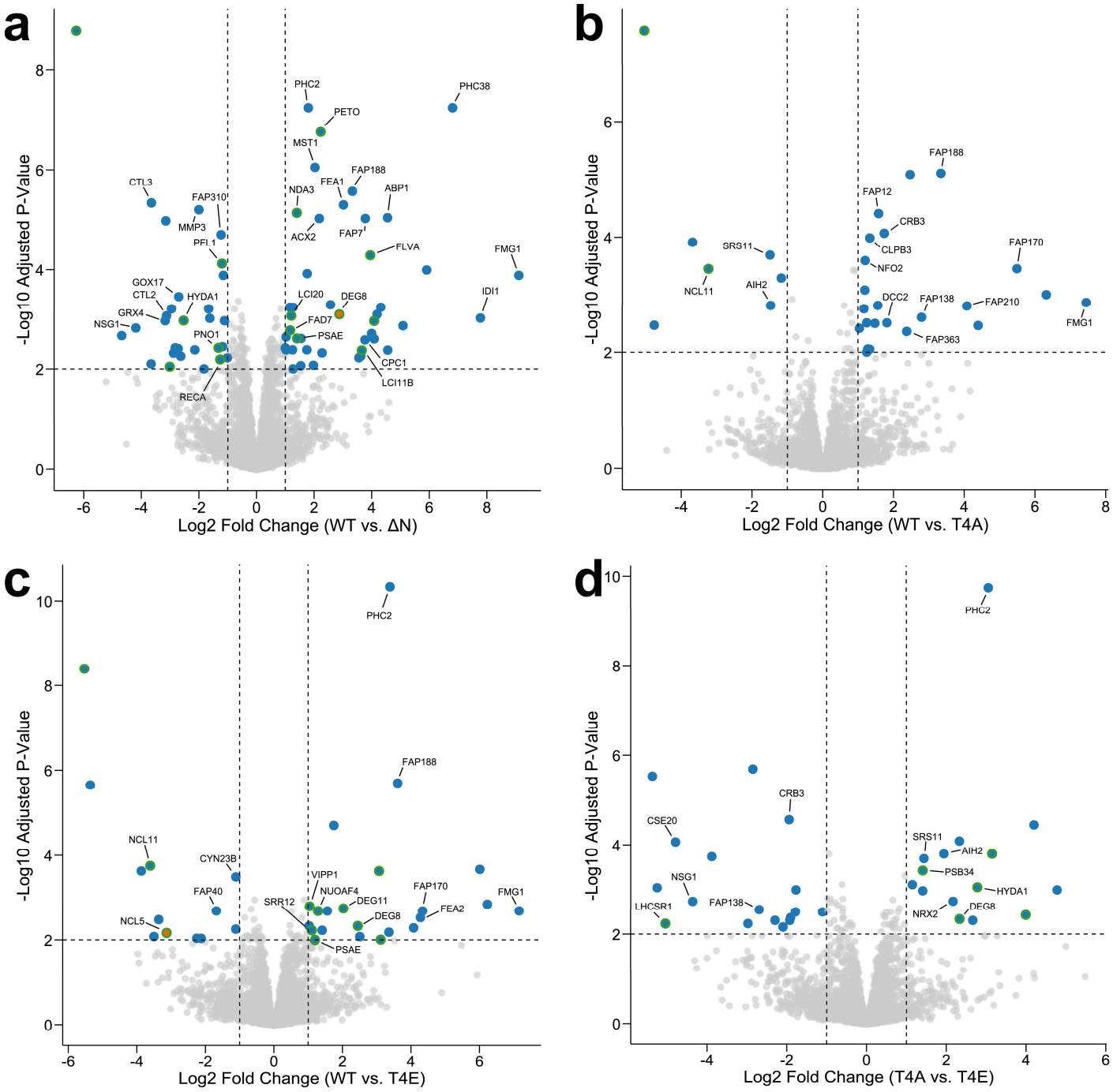

Extended Data Fig. 4. Volcano plots visualizing differential protein expression between WT and PetD mutants. Proteins from four biological replicates with FDR-adjusted p-value < 0.01 and $|\log_2$ fold change$|$ > 1 are highlighted in blue, with threshold boundaries shown as dashed lines. Data points are shown in orange instead of blue when all values for one strain in the fold-change calculation are imputed due to completely missing data. Green halos indicate chloroplast-encoded proteins and nuclear-encoded proteins with confirmed or predicted (PB-Chlamy) chloroplast localization. Comparisons are shown for **a** WT vs. ΔN, **b** WT vs. T4A, **c** WT vs. T4E, and **d** T4A vs. T4E.

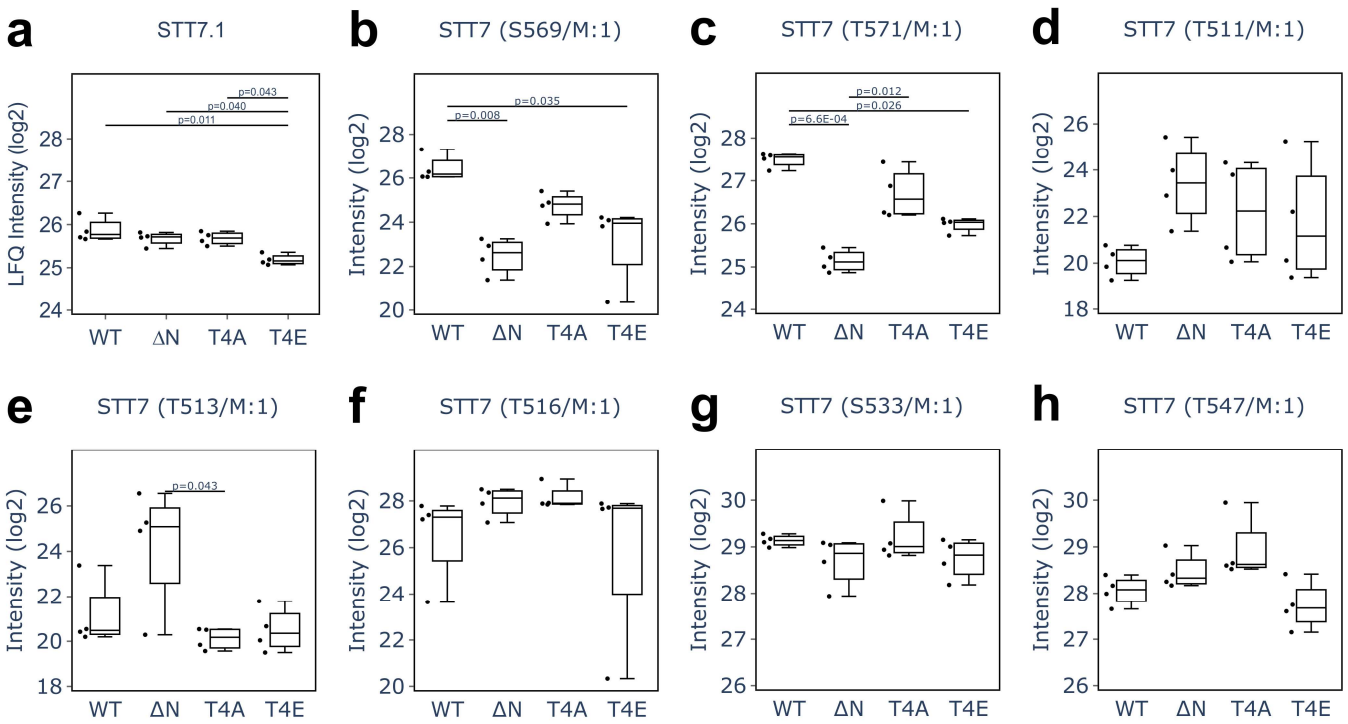

Extended Data Fig. 5. STT7 protein expression and selected autophosphorylation amounts in the engineered PetD strains. The box plots visualize significant differences of $\log_2$ fold changes in (**a**) protein LFQ and (**b**, **c**) phosphosite intensities from four biological replicates. No significant intensity differences were detectable for various STT7 phospho-peptides (panels **d** – **h**).

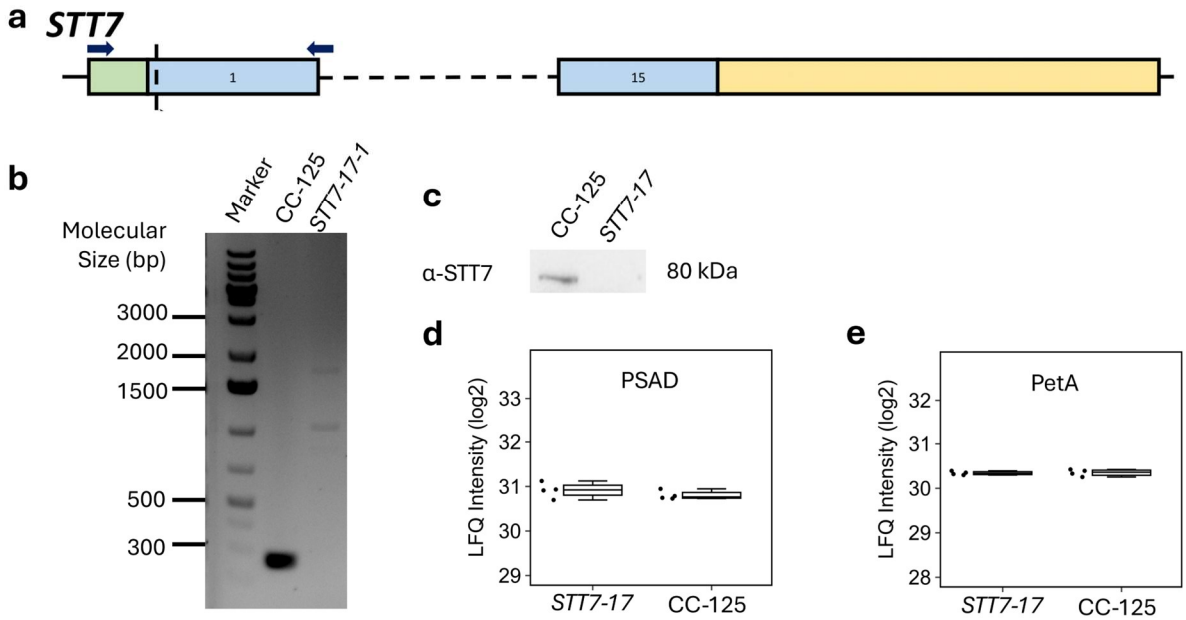

Extended Data Fig. 6. Generation of the *STT7* CRISPR/Cas mutant. a. The gene map of the *STT7* gene showing 5' UTR (green), numbered exons (blue) and 3'UTR (yellow) with predicted cut site (vertical dotted line) and primers used to verify the genotype of the insertion (blue arrows). **b.** Genetic characterization of the *STT7* mutant and its control (CC125) using PCR on genomic DNA. **c.** Immunodetection of STT7 in the *STT7* mutant and its control (CC125). The box plots in panels **d** and **e** visualize the $\log_2$ protein LFQ intensities of PSAD and PetA, respectively.

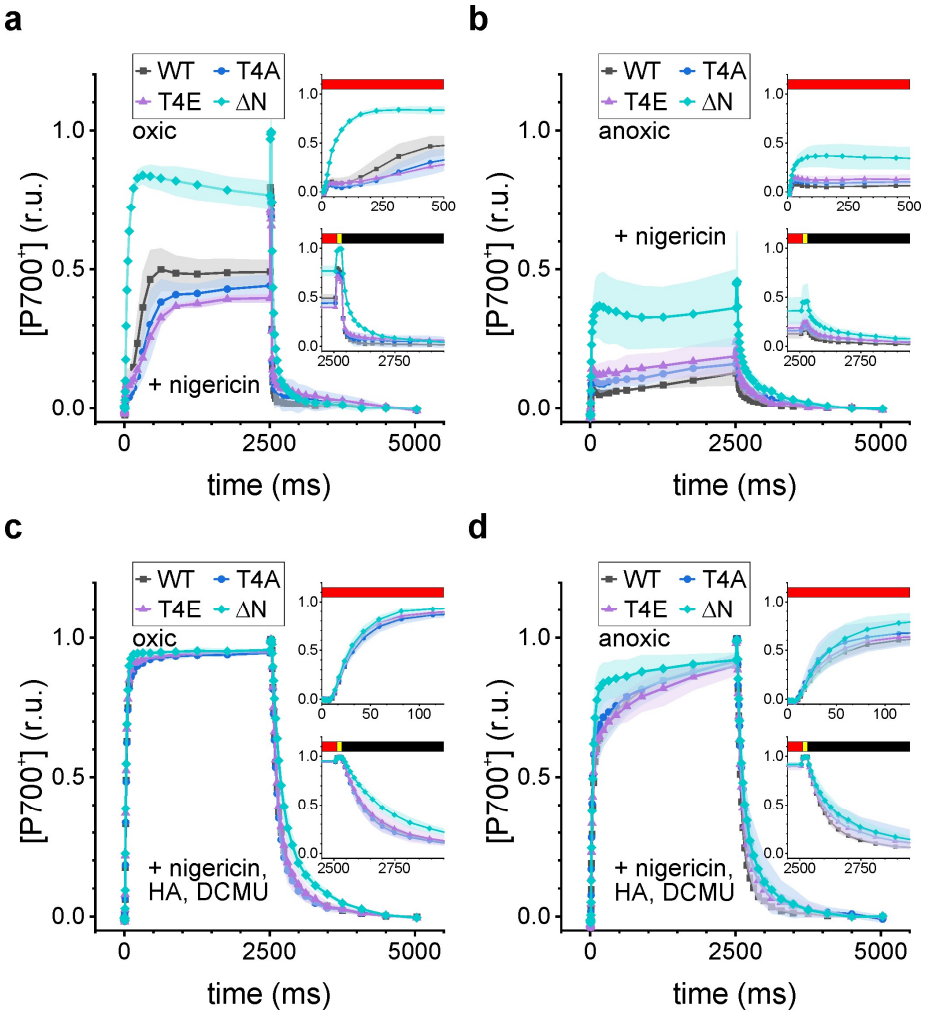

Extended Data Fig. 7. Photosynthetic activities of the cytochrome *b*$_6$*f* variants are shown for P700. Averaged kinetics are depicted (biological replicates $N = 3 \pm$ SD) and the reference measurements are shown in main text Figs. 3c and 3d. The redox changes of primary PSI donor ([P700$^+$]) is plotted (**a**) under oxic and (**b**) anoxic conditions in the presence of 10 µM nigericin, acting as H^+/K^+ exchanger to attenuate ΔpH in favor of an electric field. Red, yellow, and black bar represent actinic light intensities of 550, 3000, and 0 µmol photons m^{-2} s^{-1}. **c**, The conditions were as in panel a but photosystem II was inhibited by hydroxyl amine (HA; 2 mM) and 3-(3,4-Dichlorophenyl)-1,1-dimethylurea (DCMU; 20 µM). **d**, The conditions were as in panel c except for the anoxic pre-treatment.

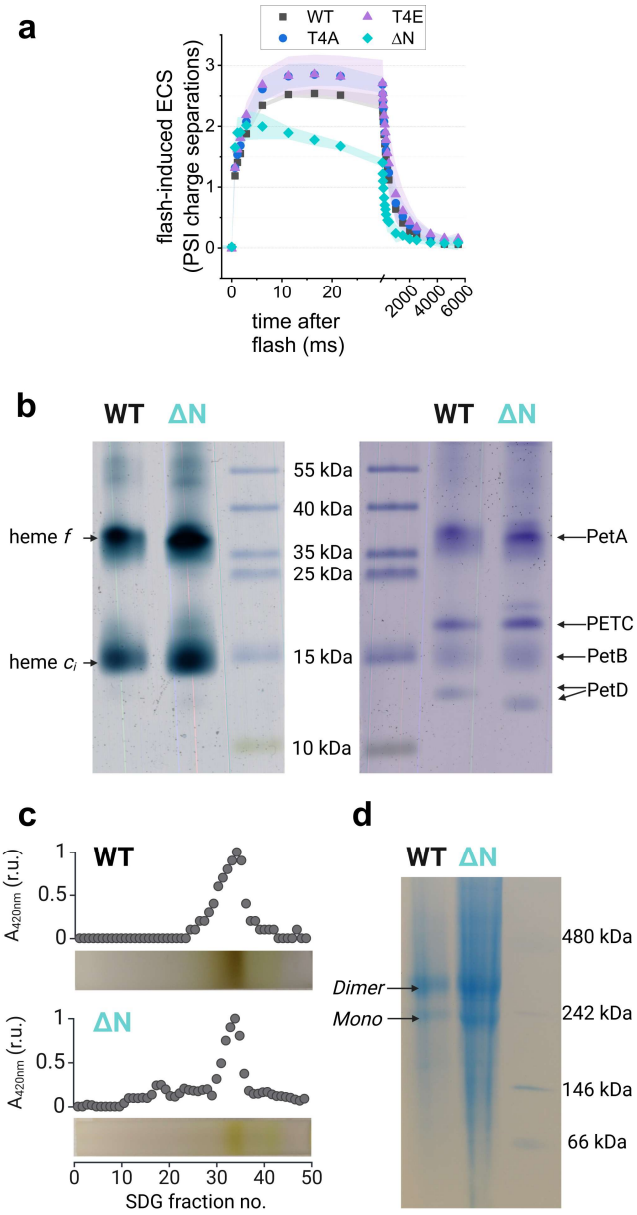

Extended Data Fig. 8. Laser flash-induced electrochromic shift (ECS) measurements show striking differences in ΔN and are not related to stability properties mutant *b*$_6$*f*. a. The ECS shows multiphasic kinetics that rely on activities of both photosystems, the cytochrome *b*$_6$*f* complex and ATP synthase. Averaged measurements are shown (biological replicates N=3 ± SD). **b.** Heme c_i was present in the ΔN mutant strain, as shown by in-gel heme staining with TMBZ. Coomassie-stained gels of 10 µg *b*$_6$*f* are shown for reference. **c.** Sucrose density gradient (SDG) fractionation and **d.** BN-PAGE analysis of 5 µg pooled *b*$_6$*f* showed no increased monomerization tendency in ΔN particles.

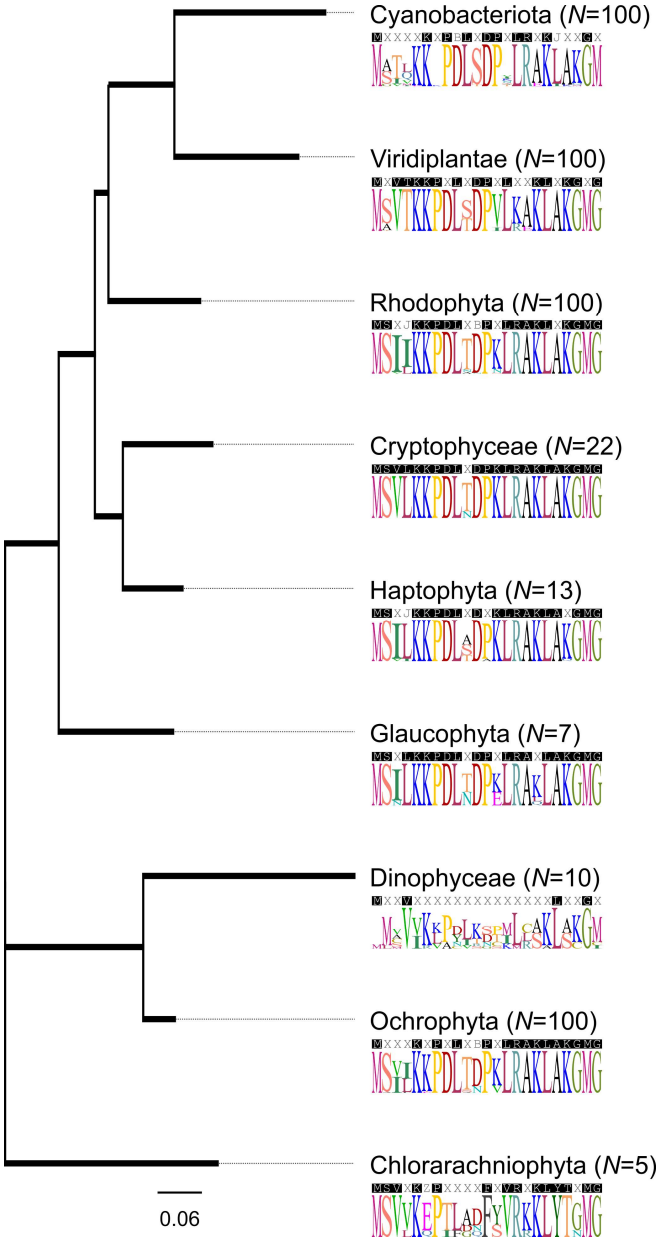

Extended Data Fig. 9. Alignments and phylogenetic tree of PetD highlights T4 in the green lineage. The consensus sequences were used for tree generation and were based on the first 100 BlastP hits (https://blast.ncbi.nlm.nih.gov/) for the *C. reinhardtii* PetD amino acid sequence. Hits were filtered for a Max Score above 100, followed removal of duplicate annotated sequences. The first 23 amino acids are shown.

768 **Extended Data Table 1. Phosphorylation data, protein fold changes, and primers for *STT7***
769 **and *petD* mutant backgrounds.** Available online.